Journal Pre-proofs

Intranasal Administration of Gold Nanoparticles Designed to Target the Central Nervous System: Fabrication and Comparison between Nanospheres and Nanoprisms

Eduardo Gallardo-Toledo, Andreas Tapia-Arellano, Freddy Celis, Tomer Sinai, Marcelo Campos, Marcelo J. Kogan, Amnon C. Sintov

PII: S0378-5173(20)30942-X
DOI: https://doi.org/10.1016/j.ijpharm.2020.119957
Reference: IJP 119957

To appear in: *International Journal of Pharmaceutics*

Received Date: 27 July 2020
Revised Date: 1 October 2020
Accepted Date: 3 October 2020

Please cite this article as: E. Gallardo-Toledo, A. Tapia-Arellano, F. Celis, T. Sinai, M. Campos, M.J. Kogan, A.C. Sintov, Intranasal Administration of Gold Nanoparticles Designed to Target the Central Nervous System: Fabrication and Comparison between Nanospheres and Nanoprisms, *International Journal of Pharmaceutics* (2020), doi: https://doi.org/10.1016/j.ijpharm.2020.119957

Research article

Intranasal Administration of Gold Nanoparticles Designed to Target the Central Nervous System: Fabrication and Comparison between Nanospheres and Nanoprisms

Eduardo Gallardo-Toledo[a,b,c,1], Andreas Tapia-Arellano[a,c], Freddy Celis[d], Tomer Sinai[b], Marcelo Campos[e], Marcelo J. Kogan[a,c,*], Amnon C. Sintov[b,*]

[a] Departamento de Química Farmacológica y Toxicológica, Facultad de Ciencias Químicas y Farmacéuticas, Universidad de Chile, Santiago 8380494, Chile.

[b] Laboratory for Biopharmaceutics, Department of Biomedical Engineering, Ben Gurion University of the Negev, E.D. Bergmann Campus, Be'er Sheva 84105, Israel.

[c] Advanced Center for Chronic Diseases, ACCDis, Santiago 8380494, Chile.

[d] Laboratorio de Procesos Fotónicos y Electroquímicos, Facultad de Ciencias Naturales y Exactas, Universidad de Playa Ancha, Valparaíso 2360001, Chile.

[e] Departamento de Química, Facultad de Ciencias, Universidad de Chile, Santiago 7800003, Chile.

[1] This work was performed in partial fulfillment of the requirements for the Ph.D. degree of E. G.-T. during his visit at Ben Gurion University of the Negev, Be'er Sheva, Israel. Parts of this manuscript were presented at the 11th World Meeting on Pharmaceutics, Biopharmaceutics and Pharmaceutical Technology, Granada, Spain.

*Correspondence to: Prof. A. Sintov, Phone: +972 8 647 2709; E-mail: asintov@bgu.ac.il

*Correspondence to: Prof. M. Kogan, Phone: +56 22 978 2897; E-mail: mkogan@ciq.uchile.cl

Abstract (200 words)

The presence of the blood-brain barrier (BBB) limit gold nanoparticles (GNP) accumulation in central nervous system (CNS) after intravenous (IV) administration. The intranasal (IN) route has been suggested as a good strategy for circumventing the BBB. In this report, we used gold nanoprisms (78 nm) and nanospheres (47 nm), of comparable surface areas (8000 vs 7235 nm^2) functionalized with a polyethylene glycol (PEG) and D1 peptide (GNPr-D1 and GNS-D1, respectively) to evaluate their delivery to the CNS after IN administration. Cell viability assay showed that GNPr-D1 and GNS-D1 were not cytotoxic at concentrations ranged between 0.05 to 0.5 nM. IN administration of GNPr-D1 and GNS-D1 demonstrated a significant difference between the two types of GNP, in which the latter reached the CNS in higher levels. Pharmacokinetic study showed that the peak brain level of gold was 0.75 h after IN administration of GNS-D1. After IN and IV administrations of GNS-D1, gold concentrations found in brain were 55 times higher via the IN route compared to IV administration. Data revealed that the IN route is more effective for targeting gold to the brain than IV administration. Finally, no significant difference was observed between the IN and IV routes in the distribution of GNS-D1 in the various brain areas.

Graphical Abstract

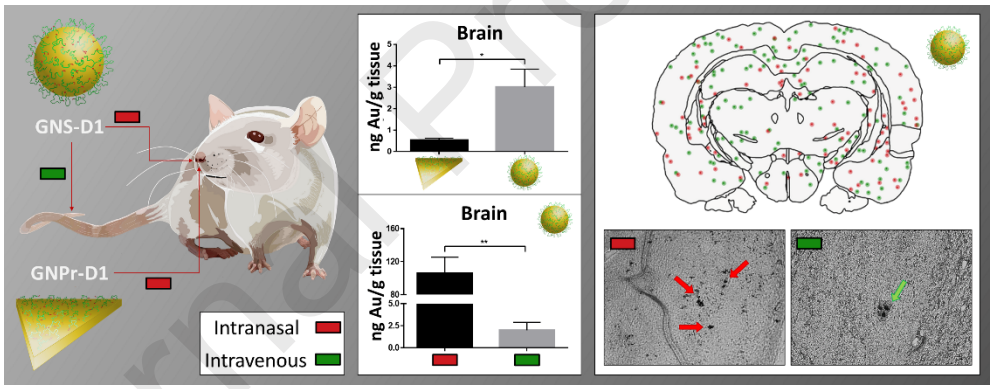

Keywords: Nose-to-brain delivery; intranasal administration; gold nanoparticles; functionalized nanoparticles; central nervous system.

1. Introduction

Gold nanoparticles (GNP) have been extensively studied for biomedical applications due to their interesting physical and chemical properties (Bergen et al., 2006; El-Sayed et al., 2005; Karhanek et al., 2005; Kohler et al., 2005). They possess a high surface area that allows adherence of various organic substances, such as drugs, peptides, and polymers. This adherence has a role in increasing the solubilization of active agents following an improvement in their pharmacokinetic parameters (Ghosh et al., 2008). GNP, like other types of nano-carriers, have a potential to specifically accumulate in tumor tissue by an enhanced permeation and retention effect (Iyer et al., 2006). However, the unique property of GNP is their ability to develop a distinct optical property known as 'localized surface plasmon resonance' (LSPR), which is caused when the surface electrons interact with electromagnetic waves. This interaction leads to a huge absorption and dissipation of local energy, which can be utilized for the destruction of tumor cells and toxic protein aggregates involved in certain pathologies. The LSPR-derived wavelength depends on the size, shape and dielectric environment of the nanoparticles (Jain et al., 2008). The LSPR band of gold nanospheres (GNS) shifts to a higher wavelength if the diameter increases, and it is commonly ranged between 515 and 560 nm (El-Sayed et al., 2005). The LSPR bands in anisotropic GNP, such as gold nanorods (GNR) or gold nanoprisms (GNPr), are largely affected by their aspect ratio and symmetry (Millstone et al., 2005). GNPr, in particular, show two main plasmons; one at 530 nm and the other is located in the near infrared region (NIR), which is the most favorable scenario for biomedical applications since biological tissues are "transparent" to these wavelengths (Weissleder, 2001).

In previous reports, our group has shown that GNP can be a potential therapy for Alzheimer's disease (AD) by disaggregation of β-amyloid (Aβ) protein aggregates and reduction of their toxicity. GNS and GNR conjugated with CLPFFD peptide, which selectively recognizes Aβ (Hetenyi et al., 2002; Soto et al., 1998), can destroy Aβ's toxic aggregates through the local release of heat produced by GNP when they are irradiated with lasers and microwaves (Adura et al., 2013; Kogan et al., 2006). A family of D-peptides, which specifically binds to $A\beta_{1\text{-}42}$ (Liu et al., 2010), has been reported to be resistant to metabolic degradation, less sensitive to proteases, and less or even not immunogenic in comparison to L-series peptides (Findeis et al., 1999). The peptide named as "D1" (peptide sequence: qshyrhispaqv) has shown to have ten thousand-fold higher affinity to Aβ than CLPFFD peptide.

Previous studies, which dealt with drug therapy for AD, were mainly based on systemic administrations, such as intravenous (IV) injection, showing a limited success due to the difficulties of crossing the blood-brain barrier (BBB). The BBB is both a defensive and highly selective barrier which isolates the central nervous system (CNS), generating a stable environment for neuronal function. Therefore, 98% of small molecules and 100% of large molecules (molecular weight > 1 kD) are not capable of crossing the BBB and reaching the CNS (Pardridge, 2007). While many studies have demonstrated a transport of metal nanoparticles through the BBB after systemic administration, the portion of the injected dose that reaches the brain was relatively low compared with other organs, such as the liver and the spleen (Frigell et al., 2014; Guerrero et al., 2010; Guerrero et al., 2012; Prades et al., 2012; Schaffler et al., 2014; Shilo et al., 2014). The low BBB transport of metal nanoparticles has also been explained by interaction of plasma proteins with the metallic surface of the nanoparticles while distributed in the body, forming the so-called 'protein corona' (Arvizo et al., 2012; Dell'Orco et al., 2010; Lundqvist et al., 2008; Monopoli et al., 2011;

Tenzer et al., 2011). The protein corona is easily recognized by macrophages, which capture the nanoparticles and contribute to the loss of a major portion after their injection, thus reducing their chance to quantitatively penetrate into the CNS. Due to this drawback, it is essential to explore alternative routes of administration of GNP to target the CNS.

One solution of bypassing the systemic organs and circumventing the BBB is the use of the intranasal (IN) route of administration, which has long been considered as an open gate for direct transport of drugs, biomarkers, and contrast agents to the brain (Dhuria et al., 2010; Illum, 2000, 2002, 2003, 2004). It has already been established that the IN route for systemic administration of many drugs has an advantage over the oral administration, due to the avoidance of the entero-hepatic metabolism and the relatively shorter onset time. The direct transport for drug from nasal cavity to the brain occurs mainly by two pathways; through the trigeminal nerve located in the respiratory region or via the olfactory region and subsequent transport into the olfactory bulbs and then to the brain (Gao, 2016). However, IN trafficking of GNP into the brain (so called 'nose-to-brain' drug delivery) has not been thoroughly explored yet, and only a few studies have been published thus far and are not focused in the effect of the shape on the delivery of particles to the CNS (Betzer et al., 2017; Hutter et al., 2010; Salem et al., 2019; Ye et al., 2018). Assuming IN delivery of GNP to the brain is effective, it would also be interesting to comprehend whether the GNP morphology is essential in its translocation from the nasal cavity to the CNS, as modifications of the physicochemical properties are known to affect the biological fate of the nanosystems (Alalaiwe, 2019; Chithrani and Chan, 2007; Chithrani et al., 2006; Hutter et al., 2010).

Our present report shows for the first time that GNS and GNPr functionalized with D1 peptide can be significantly delivered to the CNS after IN administration. Coupling of D1 peptide through formation of an amide bond, was made possible by functionalization of GNS and GNPr with a polyethylene glycol derivative HS-PEG-COOH (PEG). We also described an enrichment protocol for GNPr-PEG, designated to exclude the gold nanospheres population produced during the synthesis. The enrichment was evidenced by dynamic light scattering (DLS), spectrophotometry and transmission electron microscopy (TEM). The stability of both GNPr-D1 and GNS-D1 was assayed, and their influence on cell viability was studied in a microglial cell line. The newly developed GNP were intranasally administered to grown rats, and the quantities of gold penetrated into the brain, the olfactory bulb, and plasma were analyzed and compared. Our results showed that the brain uptake after IN administration of GNS-D1 was larger than after GNPr-D1. Finally, using only GNS-D1, we performed pharmacokinetic studies of GNP after IN and IV administration, and compared gold accumulation in brain and in various body organs (Fig. 1).

2. Materials and Methods

2.1 Materials

Gold (III) chloride hydrate, 1-ethyl-3-(3-dimethylaminopropyl)carbodiimide (EDC), and N-hydroxysuccinimide (NHS) were purchased from Sigma-Aldrich (Deisenhofen, Germany). HS-PEG-COOH MW 5KDa was purchased from JenKem Technology (Texas, USA). Isoflurane, USP 100% was obtained from Piramal critical Care, Inc. (Bethlehem, PA). Ketamine solution for injection was

obtained from Bremer pharma GMBH (Warburg, Germany), and Xylazine (as hydrochloride) 20 mg/mL solution was obtained from Eurovet Animal Health B.V. (Bladel, Netherlands).

2.2 GNPr synthesis and functionalization with PEG

GNPr were prepared by $Na_2S_2O_3$ reduction of $HAuCl_4$ by modifying the protocol described previously (Pelaz et al., 2012). Briefly, a freshly prepared 0.7 mM $Na_2S_2O_3$ solution was added to an aqueous solution of $HAuCl_4$ (2 mM). The mixed solution was allowed to react for 9 minutes then a new volume of $Na_2S_2O_3$ solution was added. The reaction was completed after 30 minutes, and the final dispersion was characterized. GNPr were functionalized with PEG (5KDa) (Morales-Zavala et al., 2017; Pelaz et al., 2012; Velasco-Aguirre et al., 2017). To achieve the chemisorption of the thiol group onto the gold nanoparticle surface, 15 µL of 0.1 mg PEG solution was added into a vial with GNPr dispersion (1 OD, pH 12) under mild stirring. The mixture was allowed to react for 3 hours, and then the vial was sonicated for 5 minutes. In order to eliminate an excess of PEG molecules, the solution was centrifuged at 5,900*g* for 20 minutes. The supernatant was discarded, and the pellet was resuspended in Milli-Q water.

2.3 GNPr's purification by centrifugation

Once GNPr were functionalized with PEG (GNPr-PEG), the samples were further purified in order to remove the gold nanospheres which had been conjointly formed during the synthesis. To achieve this goal, a centrifugation protocol was carried out (Pelaz García, 2012). GNPr-PEG dispersion denoted as "P1" was centrifuged for 20 minutes at 3,300*g*, the supernatant was discarded, and the pellet was resuspended in Milli-Q water ("P2"). Then, "P2" was centrifuged for 20 minutes at 1,500*g*, the supernatant was discarded, and the pellet was resuspended (now is "P3"). The same process was repeated to obtain "P4" (400*g*, 20 minutes), "P5" (3,300*g*, 20 minutes), and "P6" (3,300*g*, 20 minutes). All centrifugations were performed at room temperature and the samples were always sonicated before being centrifuged. Characterization of GNPr-PEG ("P6"), which was carried out by Vis-NIR spectrophotometry and TEM, has confirmed that the purification process had been completed.

2.4 Second functionalization with PEG on GNPr-PEG (P6)

GNPr-PEG ("P6") sample was re-functionalized with HS-PEG-COOH to ensure accumulation of a high number of PEG molecules on the GNPr surface. An aliquot of 150 µL of 0.2 mg PEG solution was added to 1 OD solution of "P6" (pH 12). The functionalization was carried out overnight under mild stirring at room temperature. Afterwards, the sample was sonicated and centrifuged at 3,300*g* for 20 minutes. The supernatant was discarded, and the pellet was resuspended in Milli-Q water (GNPr-PEGx2).

2.5 GNS synthesis and functionalization with PEG

Citrate-coated gold nanospheres (48 nm) were prepared by citrate reduction of $HAuCl_4$, according to the Turkevich method (Turkevich, 1985). An aqueous solution of $HAuCl_4$ (0.01% w/v) was heated to boiling, then a warm (50–60°C) aqueous solution of sodium citrate (1% w/v) was quickly added. The reaction took place 15 minutes under magnetic stirring until a deep purple solution was obtained. The dispersion was cooled down to room temperature, and then characterized. To modify the surface with PEG, 1 OD-GNS dispersion was allowed to react with 300 µL of PEG (5 mg/mL) solution, under mild stirring, for 1.5 hour. Then the mixture was sonicated for 5 minutes and centrifuged for 20 minutes at 5,900*g*. The supernatant was discarded, and the pellet was resuspended in Milli-Q water.

2.6 Conjugation of GNPr-PEGx2 and GNS-PEG with D1 peptide

By a reaction of the gold nanoparticles with EDC/NHS, amide bonds were generated between the carboxylate groups of PEG and the amine groups of D1 peptide (Morales-Zavala et al., 2017; Velasco-Aguirre et al., 2017). D1 peptide was synthesized and obtained as previously described (Morales-Zavala et al., 2017). GNPr-PEGx2 and GNS-PEG were first centrifuged for 20 minutes (3,300*g* and 5,900*g*, respectively) and the pellets obtained were resuspended in 400 µL of Milli-Q water. Then, an aliquot of 100 µL of EDC/NHS was added to activate the carboxylic groups. The amounts of EDC/NHS for GNPr-PEGx2 and GNS-PEG were 0.9/1.35 mg and 1/2.5 mg, respectively. Both samples were allowed to react for 15 minutes under orbital agitation. The samples were sonicated and centrifuged for 20 minutes at 3,300*g* (GNPr) and 5,900*g* (GNS) to remove the excess of EDC/NHS molecules. The pellets were resuspended in 700 µL of PBS, and then 100 µL of D1 solution (3 mg/mL) were added to the activated GNPr and GNS. The samples were sonicated for 5 minutes and then incubated overnight at room temperature under orbital agitation. Finally, GNPr-D1 and GNS-D1 were re-centrifuged, pellets were resuspended in Milli-Q water and stored at 4°C.

2.7 UV-Visible-NIR spectrophotometry

Absorption spectra were recorded at room temperature in Milli-Q water using a Perkin Elmer Lambda 25 spectrophotometer. Each spectrum was used to determine and observe the characteristic plasmon bands of naked GNPr and GNS, and their respective functionalized forms.

2.8 Dynamic Light Scattering (DLS)

Hydrodynamic diameter and colloidal stability of all samples were measured using a Malvern ZetaSizer 3000 (Malvern Instruments, UK). An aliquot of each sample was placed in a disposable polycarbonate capillary cell (DTS 1061) and measures were conducted at a wavelength of 633 nm, fixed scattering angle of 173°, and under precise temperature control (25°C).

2.9 Nanoparticle tracking analysis (NTA):

Measurements were performed using a NanoSight NS300 instrument (Malvern Instruments Ltd, Worcestershire, UK), equipped with a 405nm laser module and 450nm long-pass filter, and a camera operating at 25 frames per second, capturing a video file of the particles moving under Brownian motion. The software for capturing and analyzing the data (NTA 2.3) calculated the hydrodynamic diameters of the particles by using the Stokes–Einstein equation. In addition to size measurements, the instrument also measures the concentration of the particles in the sample (see below).

2.10 Zeta potential (Z.P.)

Z.P. measurements were carried out in a ZetaSizer 3000 (Malvern Instruments, UK) at 25°C. As samples were in aqueous media, Smoluchowski approximation was used to calculate Z.P. values.

2.11 Transmission Electron Microscopy (TEM)

The size and morphology of gold nanoparticles were determined by electron microscopy using a FEI Tecnai G^2 TWIN transmission microscope, operating at 120 kV. The grids were prepared by dropping a GNPr or GNS dispersion onto a Formvar carbon-coated copper microgrids and drying them after 5 minutes. The samples were stained with phosphotungstic acid 1% in order to observe the organic material over the surface.

2.12 Determination of gold nanoparticle concentrations

To determine the number of nanoparticles per milliliter, NTA was performed with a NanoSight NS300 (Malvern Instruments, UK), and NanoSight software version NTA 3.2 was used for data accumulation and analysis. NTA is a fast approach that can be used for quantitative measurements. A linear relationship was established between the nanoparticle concentrations and the absorbance values of plasmon bands. Five samples of GNPr-D1 or GNS-D1 with different absorbance values, ranging between 0.1 and 1.0, were diluted and measured. Data were recorded using a camera level of 15, 50-second video clips, and a detection threshold of 3. A red laser (642 nm) was used for GNPr-D1 and GNS-D1 measurements. All measurements were carried out in Milli-Q water at a temperature of 25°C.

2.13 Number of D1 peptide molecules per nanoparticle

Amino acid analysis was used to estimate the number of D1 peptide molecules in samples of known GNPr or GNS concentrations (Morales-Zavala et al., 2017; Velasco-Aguirre et al., 2017). The concentration was determined by nanoparticle-tracking analysis (NanoSight, see above). Samples were concentrated by centrifugation (5,900*g* x 20 min) to obtain 40 µL dispersions. α-Aminobutyric acid (AABA) solution (2.5mM, 12 µL) of was added as an internal standard. Samples were hydrolyzed for 72 h in 6N HCl, evaporated and resuspended in 20mM HCl to a final volume of 200 µL. For each stock, 20 µL were taken and mixed with 60 µL of borate buffer.

The amino acids in the hydrolysate were derivatized by adding 20 µL of 6-aminoquinolyl-n-hydroxysuccinimide-activated heterocyclic carbamate (Waters AccQ·Fluor™ Reagent), and allowed to react for 1 min at room temperature followed by 10 min at 55°C. Samples were injected in a HPLC-PDA instrument with a AccQ-Tag column (C18; 4 µm; 3,9 x 15 mm). Peaks obtained were compared with amino acid standards (Waters Pico-Tag), and the concentration of the peptide was determined.

The number of peptide molecules/mL were divided by the number of gold nanoparticles/mL in order to obtain the number of peptide molecules per nanoparticle:

$$N = \frac{Peptide\ (\mu M)}{NP\ (nM)} \times 1000$$

N: number of D1 peptide molecules per nanoparticle

Peptide: Concentration of D1 peptide (µM) determined by the amino acid analysis.

NP: Concentration of nanoparticles (nM; GNPr or GNS) determined by NanoSight.

2.14 Raman spectroscopy

All the Raman spectra of samples containing D1 peptide, GNPr-D1 and GNS-D1, were registered with a Renishaw InVia Raman spectrometer. The micro-spectrometer was equipped with the 785 nm laser line, electrically cooled CCD detector and coupled to a Leica microscope DMDL. The Raman signal was internally calibrated to the 520 cm^{-1} line of silicon. The spectral range was set between 200-2000 cm^{-1} and the number of acquisitions was 1 at 10 s of integration time. The laser power was 0.2 mW (less than 1%) in order to avoid any photodecomposition. The samples were deposited on a thin sheet of gold to remove the intrinsic fluorescence. This surface was prepared by depositing Au film in Argon plasma on a glass substrate by the sputtering method. The Raman spectra of D1 was registered in the solid state, while the SERS spectra of the GNPr-D1 and GNS-D1 were obtained after evaporating the solvent without any light exposition.

2.15 Stability assays

To determine the colloidal stability of GNPr-D1 and GNS-D1, different assays were carried out. All samples were characterized by UV-Visible-NIR spectrophotometry, DLS, and Z.P.. Each condition was evaluated in independent experiments and in triplicate. GNPr-D1 and GNS-D1 dispersions in Milli-Q water were stored at 4°C for a period of 28 days. Their physicochemical parameters were evaluated on day 1, 7, 14, and 28. The stability of GNPr-D1 and GNS-D1 were also determined when samples were resuspended in Milli-Q water, PBS, or a culture medium (RPMI-1640, Biological Industries, Beit HaEmek, Israel) for a period of 24 h at 37°C. Physicochemical properties were determined at time zero (T0) and after 24 h (T24). Before measurements, diluted samples in Milli-Q water, PBS, and RPMI were centrifuged and resuspended in Milli-Q water for characterization.

2.16 Cell viability

To determine the effect of GNPr-D1 and GNS-D1 on cell viability, the tetrazolium salt reduction assay (XTT) was performed. This assay establishes a linear relationship between the number of viable cells and absorbance. BV-2 microglial cells were seeded on 96-well plates at a cell density of 20,000 cells/well. BV-2 cells were seeded using RPMI-1640, FBS 10%, and L-glutamine. Then, the cells were treated with increasing concentrations of GNPr-D1 and GNS-D1. After 24 h of incubation, cell viability was measured (in triplicate) in three independent experiments using the tetrazolium salt reduction assay according to manufacturer's protocol. XTT tetrazolium salts were mixed with an electron coupling reagent (phenazine methosulfate; PMS). The mixture was added to the cells from 1 to 4 h at 37 °C. The absorbance at 455 nm was monitored on a Multiscan reader with a reference wavelength of 660 nm.

2.17 *In vivo* experiments

2.17.1 *Animals*

All animal treatments and experiments were performed in accordance with protocols reviewed and approved by the Institutional & Use Committee, Ben- Gurion University of the Negev, which complies with the Israeli Law of Human Care and Use of Laboratory Animals. Sprague-Dawley rats (male, 350-400g body weight, Envigo RMS, Ein Karem, Jerusalem) were used in this study. All animals were housed in polycarbonate cages and maintained on a 12/12 h light/dark cycle under controlled conditions of temperature and humidity. The rats had free access to food and water.

2.17.2 *IN administration of GNPr-D1 and GNS-D1*

Animals were randomly divided into two groups of three animals each for GNPr-D1 and GNS-D1. The dose administered to each animal was $4.5x10^{11}$ nanoparticles/Kg of body weight. The administered volume was 75 µL/Kg of body weight (37.5 µL per nostril/Kg body weight). The animals were sedated with isoflurane inhalation just before administration. After 30 minutes from administration, the animals were deeply anesthetized with ketamine (80mg/Kg, i.p.) and xylazine (10mg/Kg, i.p.). Then, 0.5 mL of blood was taken from the right atrium and transcardial perfusion was carried out with PBS to eliminate residual blood from body organ. Brain and olfactory bulb were then removed, washed with PBS, frozen at -80°C, lyophilized overnight, and weighed.

2.17.3 *Pharmacokinetic study of GNS-D1*

Fifteen animals were randomly divided into five groups of three rats each. The administered dose used in this experiment was the same as described above ($4.5x10^{11}$ nanoparticles/Kg; 37.5 µL volume per nostril/Kg). The rats were sacrificed at 0.75, 2, 4, 8, and 24 h after administration following the same procedure described previously. A volume of 0.5 mL of blood was collected from the right atrium and brain, olfactory bulb, and liver were removed, washed in PBS, frozen at -80°C,

and lyophilized. Then, all dried organs were grinded, and a known weighted amount was analyzed (see below) to determine the gold content.

2.17.4 *Comparison between IN and IV administrations of GNS-D1*

Animals were randomly divided into two groups of three animals each for IN and IV administrations. The administered dose (nanoparticles/Kg) was the same as applied in the previous experiments. Via the IN route, the volume administered was 75 µL/Kg of body weight (37.5 µL per nostril/Kg body weight), whereas via the IV route (tail vein), the injected volume was 1,230 µL/Kg of body weight. The animals were sedated with isoflurane inhalation prior to IN or IV administration. After 0.75 h from administration, the animals were deeply anesthetized with ketamine (80mg/Kg, i.p.) and xylazine (10mg/Kg, i.p.). Then, 0.5 mL of blood was taken from the right atrium and transcardial perfusion was carried out with PBS to eliminate residual blood from the body organs. Brain, olfactory bulb, liver, spleen, and lungs were then removed, placed and washed with PBS, frozen at -80°C, and lyophilized until they were completely dry.

2.17.5 *Gold quantification in body tissues*

i) Induced coupled plasma mass spectroscopy (ICP-MS 7500cx, Agilent Technologies, The Hebrew University of Jerusalem, Jerusalem, Israel) was used to determine the amount of gold in each sample. Freeze-dried organs were melted and digested with H_2SO_4 (96%), HNO_3 (70%), and H_2O_2 (30%) until a clear liquid is obtained. To disintegrate the gold nanoparticles, samples were digested with *aqua regia* (HCl:HNO_3, 3:1) and H_2O_2. The solutions were then evaporated and diluted with 5 mL of distilled water. Gold concentrations were determined according to absorbance values, which were correlated with the calibration curves (0.1 to 10 ppb). The detection limit of the instrument was 0.01 ppb.

ii) Only for the pharmacokinetic study, the amount of gold was determined by Neutron Activation Analysis (NAA) at the Comisión Chilena de Energía Nuclear (CCHEN), as was previously described (Velasco-Aguirre et al., 2017). Briefly, the samples were sealed by friction welding and exposed for 17 h to a neutron flux of 0.25–1.3 x 1013 n/cm^{2}s with a power of 5 mW using a RECH-1 reactor at the CCHEN, thereby the conversion of ^{197}Au to ^{198}Au was triggered. After 7–12 days of decay, the γ-rays emitted by the samples were measured using a germanium detector coupled to a PC-based multichannel γ-ray spectrometer. The γ-spectra were analyzed using the software SAMPO90 Canberra. Gold standards were run together with the experimental samples to standardize a library of gold element data from which the amount of gold content in the unknown samples was calculated.

2.17.6 *Brain distribution of GNS-D1*

To determine the GNS-D1 distribution in brain, four animals were randomly divided into two groups of two rats each. One group was intranasally administered, whereas the other received an IV bolus injection. The same procedures for sedation, administration, and anesthesia that were previously

described were also applied to this experiment. After transcardial perfusion with PBS, the brains and olfactory bulbs were extracted and fixed with 4% formaldehyde solution at 4°C overnight. Then, they were washed and placed in 30% sucrose in PBS until the tissues sank. Brains and olfactory bulbs were embedding in OCT and sectioned (coronary plane) at 4 µm thickness using LEICA CM 1950 cryostat. The tissue distribution and localization of GNS-D1 was carried out using the GoldEnhance™ kit for light microscopy, following reports that have used this particular kit (Ng et al., 2015; Talamini et al., 2017). Under light microscopy, GNS-D1 were identified as black granular pigments, which were not found in control organs (i.e., untreated with GNS-D1). Brain localization of each gold cluster were assigned using the Waxholm rat atlas as reference (Kjonigsen et al., 2015; Papp et al., 2014; Sergejeva et al., 2015). More than four hundred of gold cluster were found for each route of administration. The percentage of localization was calculated using the total number of clusters per route of administration as 100%.

3. Results and Discussions

3.1 GNPr synthesis and functionalization

GNPr were synthesized following a modified protocol described previously (Pelaz et al., 2012). The protocol was based on a two-step process, in both the gold (III) salt solution is reduced by reacting with $Na_2S_2O_3$. After 9 min of the first step, a second addition of $Na_2S_2O_3$ (0.7 mM) is performed, yielding GNPr. Fig. 2 shows the GNPr spectrum, in which two plasmon bands are observed, one at 530 nm and other in the NIR at 845 nm. As described by Pelaz et al., 2012, the former plasmon corresponds to the plasmon associated with the nanoprism's width and with the gold nanospheres (a byproduct), whereas the latter is related to the nanoprism's length. GNPr size was measured by DLS, obtaining an average hydrodynamic diameter of 52 ± 4 nm, and an average Z.P. of -44 ± 2 mV (Table 1).

Table 1. Physicochemical characterization of GNPr, GNPr-PEG (from P1 to P6), GNPr-PEGx2, and GNPr-D1. Nanoprisms were characterized at each functionalization and purification step, and the values for plasmon bands, hydrodynamic diameter, and Z.P. were determined. Percentage of GNPr and GNS were determined according to TEM images.

Sample	Plasmon Band (nm)		Hydrodynamic diameter (nm)	Z.P. (mV)	GNPr/GNS ratio
	Vis	NIR			
GNPr	530	845	52 ± 4	-44 ± 2	35/65
P1	530	848	68 ± 7	-36 ± 2	42/58
P2	530	849	70 ± 7	-35 ± 4	54/46
P3	531	860	66 ± 8	-37 ± 4	56/44
P4	531	876	69 ± 5	-36 ± 5	58/42
P5	531	905	81 ± 8	-32 ± 9	70/30
P6	531	910	89 ± 1	-33 ± 4	79/21
GNPr-PEGx2	531	915	92 ± 5	-41 ± 1	80/20
GNPr-D1	531	920	108 ± 3	-25 ± 2	70/30

The next process, which was carried out after GNPr synthesis, was their functionalization with PEG (Mw 5 kDa). The process stabilized the colloid and enabled D1 peptide to bind on the surface

through a reaction with -COOH groups. The thiol groups interact with the gold surface producing a chemisorption of PEG molecules. After 3 hours of functionalization under mild stirring, GNPr-PEG were obtained. Table 1 shows the spectra obtained after the addition of PEG and PEG-D1. An increment of 16 nm in the hydrodynamic diameter of GNPr-PEG (P1) resulted in a red-shift of 3 nm in the NIR-plasmon band. The shift was gradually grown during the purification/enrichment process (more details are provided in the following section 3.2). The Z.P. of P1 turned to be slightly less negative, with a value of -36 ± 2 mV.

3.2 GNPr-PEG enrichment

Due to the high quantity of gold nanospheres, which was produced during the synthesis of gold nanoprisms, a purification protocol was carried out to reduce this byproduct. The process was adapted from Pelaz García, 2012 that involved six successive centrifugations in which the supernatant was discarded, and the pellet was re-suspended in milli-Q water. Every step was monitored by spectrophotometry, DLS, and TEM to follow up the enrichment of GNPr-PEG. It should be noted that it is necessary to functionalize GNPr with PEG before the enrichment process because the naked GNPr are unstable and tending to aggregate when the solvent is replaced. To follow up the enrichment process, we monitored each centrifugation step by Vis-NIR spectrophotometry. As shown in Fig. 3a, we observed a red-shift of the plasmon after each centrifugation step, moving from 848 (P1) to 910 nm (P6). In addition, we observed a decline in the intensity of Vis-band plasmon of the GNPr-PEG from one centrifugation step to the next. Since the Vis-band plasmon is attributed to the GNS signal, its drop indicates how GNPr enrichment is progressed, evidenced by a reduced GNS in P6 compared to P1. As a consequence of the decay in the Vis-band at 530nm, the nanoparticles changed their color from purple to gray-green in P1 and P6, respectively (Fig. 3b). Evidently, as the proportion of the red-purple colored GNS in the system was reduced, the gray-green colored GNPr became more dominant. In addition, a statistical analysis of the GNPr-PEG population was performed (Table 1), showing that the proportion of prisms/spheres increased from 42/58 to 79/21 for P1 to P6, respectively. This analysis confirmed that the decrease in the intensity of the Vis plasmon band was related to the percentage of GNS population in the system. Considering a significant enrichment of GNPr-PEG in P6, further functionalization was therefore carried out.

Every step of GNPr-PEG enrichment process was also followed up by measurements of hydrodynamic diameters of the particles as well as their Z.P. (Table 1). Measurements have shown an increase in the hydrodynamic diameter from 68 ± 7 to 89 ± 1 nm for P1 and P6, respectively. This tendency of increase in the mean size of the GNPr-PEG during the enrichment process was consistent with the Vis-NIR spectra and the bathochromic shift of the GNPr's NIR-plasmon through this process. The Z.P. obtained for P1 and P6 showed values of -36 ± 2 and -33 ± 4 mV, respectively, and actually remained constant through the enrichment process from P1 to P4, then dropped to 32 and 33 mV in P5 and P6. This negative charge on the GNPr surface of P1 or P6 was due to ionization of the carboxylic acid end-groups at the PEG moieties.

TEM imaging of GNPr-PEG for each centrifugation/enrichment step was created to visualize the presence of GNPr-PEG and to statistically analyze the size and population proportions of GNPr-PEG (Fig. S1 & 3c-d). Interestingly, TEM images of samples P1-P6 showed an increase in the mean particle length of the GNPr-PEG from 51 to 70 nm of P1 and P6, respectively. This increase in GNPr size is

associated with the shift of the NIR plasmon band, which means that as larger the GNPr is, the greater are the bathochromic and hydrodynamic changes.

3.3 Double-PEG functionalization and D1 conjugation

After the enrichment process, GNPr-PEG was re-functionalized for the second time to ensure the presence of a higher surface density of PEG molecules (Huang et al., 2010; Liu et al., 2015). This additional step was carried out since a large portion of PEG molecules had actually been wasted by binding onto GNS and removed during enrichment. Therefore, it was essential to attach more PEG molecules on the GNPr surface that would create more binding sites for D1 peptide. GNPr-PEG were incubated with a PEG solution and then centrifuged and resuspended in water (GNPr-PEGx2). Vis-NIR spectrum showed a gradual shift in the longitudinal plasmonic band (Fig. 2a and Table 1) from 845 (GNPr) to 910 (GNPr-PEG), and to 915 nm (GNPr-PEGx2). DLS measurements showed an increase in the hydrodynamic diameter from 89 to 92 nm, whereas Z.P. decreased towards more negative value, from -33 to -41mV from GNPr-PEG to GNPr-PEGx2 (Table 1). The bathochromic shift, the increase in the hydrodynamic diameter, and the decrease in the Z.P. value suggest that the second functionalization process enhances the surface density of PEG on the GNPr. To determine the size and population of GNPr-PEGx2, TEM images were used to complete the characterization of this sample. According to TEM observations, the mean length enhances from 70 (GNPr-PEG) to 79 nm (GNPr-PEGx2) (Fig. 3d and 2c). The population of GNPr-PEGx2 in a dispersion remained at the same proportion as had been before the second functionalization (Table 1).

The incorporation of D1 peptide onto the GNPr-PEGx2 surface was performed by a reaction with the carboxylate end-groups of the PEG. These end-groups and the amino groups of D1 peptide were reacted in an aqueous medium to form amide bonds. As a consequence of this conjugation, a shift in the NIR plasmonic band was observed from 915 to 920 nm, the hydrodynamic diameter (according to DLS analysis) was increased from 92 to 108 nm, and the Z.P. had a notable change from -41 to -25 mV (Table 1). These data confirm that the binding reaction of D1 peptide on the surface of GNPr-PEG occurs since the measurements of Z.P. were performed at pH 5.5 while the isoelectric point of the peptide is 8.76. Interestingly, the size of GNPr-D1 as observed by TEM was 78 ± 18nm (average length) (Fig. 2d), which was similar to the size of its precursor GNPr-PEGx2, implying that the new functionalization with D1 peptide is not observable by TEM. The reason for the discrepancy between TEM observation and DLS analysis is explained by the image obtained by TEM correspond to the gold core of the nanoparticle as compared to the hydrodynamic method of the DLS. Also, the GNPr-D1 population (compared to GNPr-PEGx2 population) decreased from 80% to 70%, which was due to the covalent coupling with EDC/NHS causing to adherence of some activated GNPr onto the surface of centrifuge tubes. The results have clearly demonstrated that D1 peptides were anchored and functionalized to the PEG on the GNPr surface.

3.4 GNS preparation and functionalization

GNS were synthesized by using the Turkevich's method of reducing a gold salt solution with sodium citrate (Turkevich, 1985). The obtained nanoparticles showed a plasmon band at 532 nm and had a hydrodynamic diameter of 65 ± 9 nm and a Z.P. of -21 ± 1 mV (Table 2). Like GNPr, GNS were

functionalized with PEG by mixing of a GNS dispersion with PEG solution. After centrifugation and reconstitution of the pellet, a GNS-PEG dispersion was obtained, showing a red shift of 1 nm in the plasmon band (Fig. 4a and Table 2). The hydrodynamic diameter increased by 27 nm and the Z.P. was turned to be more negative with a value of -34 ± 1 mV (Table 2). D1-peptide molecules were functionalized as described above for GNPr-D1. A red-shift of 1 nm in the plasmon band was observed in GNS-D1 compared to GNS-PEG, and 2 nm shift compared to non-functionalized GNS (Fig. 4a and Table 2). In addition, the hydrodynamic diameter increased to a value of 99 ± 5 nm, and the Z.P. became more positive (from -34 ± 1 to -31 ± 2 mV, Table 2). TEM images were also taken to evaluate the morphology, size distribution, and diameter of the nanoparticles (Fig. 4). GNS exhibited a mean diameter of 47 ± 9 nm (Fig. 4b). Unlike naked GNS, images of GNS-PEG and GNS-D1 were observed with a "halo" circled around the spheres. Taking the "halo" layer into consideration, the mean diameter of GNS-PEG was 54 ± 8 nm (Fig. 4c), and GNS-D1 diameter was 57 ± 11 nm (Fig. 4d). The mean diameter of the gold core remained constant after the functionalization steps. After the functionalization with PEG, the mean diameter (with the halo) increased by 7 nm only. According to DLS measurements, the length of a completely stretched-out PEG molecule (5 kDa) is 27 nm (Cauda et al., 2010). That means that the difference of 20 nm observed between the stretched-molecular length and the mean halo length as observed by TEM may be explained by folding and entanglements of PEG chains over the nanoparticle surface (Steinmetz and Manchester, 2009). After the binding of D1 peptide, nanoparticles increased in size by additional 7 nm in diameter according to the DLS measurement, while TEM observation revealed only an increase of 3 nm in diameter, which is approximately fitted with the peptide's length (3.8 nm). Like the GNPr production, the physicochemical changes of functionalization were monitored as an indication for process follow-up and for verification that each step had been completed. When GNS were functionalized with PEG, the Z.P. received a significant negative value due to the contribution of the additional HS-PEG-COO^- groups to the triple negatively charged groups of the citrate molecules (used for reduction of the gold salt). Since the number of the bound citrate molecules after GNP are formed as well as the number of PEG molecules after functionalization are unknown, thereby the large decline in the Z.P. after the addition of PEG molecules onto the GNS surface can be used as an important in-process information. In comparison to the functionalization of GNPr-PEGx2 to GNPr-D1, in which the Z.P. increased from -41 to -25 mV (16 mV difference), the observed change in Z.P. from GNS-PEG to GNS-D1 was relatively minor with only 3 mV increase (from -34 to -31 mV). Therefore, amino acid analysis was carried out to ascertain the conjugation of D1 peptide molecules to the GNS-PEG surface (see section 3.5 below).

Table 2. Physicochemical characterization of GNS, GNS-PEG, and GNS-D1. The values for plasmon bands, hydrodynamic diameter, and Z.P. were evaluated for each nanosystem.

Sample	Plasmon band (nm)	Hydrodynamic diameter (nm)	Z.P. (mV)
GNS	532	65 ± 9	-21 ± 1
GNS-PEG	533	92 ± 4	-34 ± 1
GNS-D1	534	99 ± 5	-31 ± 2

3.5 Disposition of D1 peptide over the surface of GNPr and GNS

To evidence that functionalization and disposition of D1 peptide really occurred on the surface of GNPr and GNS, amino acid analysis and Raman spectrometry were performed. According to the nanoparticle concentration obtained by NTA and the amino acid analysis, the number of peptide molecules per one gold nanoparticle was determined and calculated, 1300 and 4800 molecules per GNPr and GNS, respectively. According to the mean length and width of GNPr and the diameter of GNS obtained by TEM, we calculated their surface areas, which were approximately 8000 nm^2 for GNPr and 7235 nm^2 for GNS. Based on their similar surface areas, and as the number peptide molecules depends on the number of PEG molecules on the surface, it seems that the degree of functionalization of PEG on each type of nanoparticles was different, i.e., higher functionalization of D1 peptide on GNS than on GNPr.

To determine the disposition of the D1 over the gold surface, Raman spectrum was first obtained for D1 peptide (Fig. 5a-i), which exhibited characteristic signals at 1440, 1274, 1212, 854, 837, 725, 643, 598 and 407 cm^{-1} with a medium-strong relative intensity. Proposed bands assignment is detailed in Table S1 and based on published related data (Aliaga et al., 2011; Aliaga et al., 2010; Culka et al., 2010; Garrido et al., 2012; Long, 2004; Vera et al., 2015; Zhu et al., 2011). According to these publications, the guanidino group of arginine (R) is observed at 1440 cm^{-1}, while other bands of the same amino acid are observed at 1051, 991 and 924 cm^{-1} with variable intensities. Vibrations of tyrosine (Y) are observed at 1274, 837, and 643 cm^{-1}. In particular, the band at 837 cm^{-1} with a strong relative intensity is assigned to a CCN vibration of Y. The signal associated with serine (S) with medium relative intensity is observed at 1212 cm^{-1}. A coupling vibration of identical modes of tyrosine and alanine (A) is observed at 854 cm-1; A also displays a weak band at 598 cm-1 which is assigned to the carboxylate deformation group. Other amino acids bands belonging to glutamine (Q) and histidine (H) are observed in the Raman profile of D1. Characteristics bands of Q are located at 1677 and 1620 cm^{-1} while H is inferred from the appearance of the band at 725 cm^{-1}. Finally, the band at 407 cm^{-1} is ascribed to deformation modes involving the CN structural moiety.

The Raman spectrum of GNS-D1 displayed just a few signals of the amino acids that constitute the D1 peptide (Fig. 5a-ii). In this sense, R, Y, H, S, and A were the amino acids identified in the spectrum, providing information about the sequence part of the D1 peptide that interacted with the gold surface. Therefore, the *qshyrh* sequence was the most representative fraction of D1 and its orientation was closer to the gold surface than the sectional tail composed by the *spaqv* sequence (Fig. 5b, right). Additionally, wavenumber shift of some bands suggests a new conformation of D1 on the GNS surface, as in the case of Q that appeared at 1620 cm^{-1} in the Raman spectrum of D1 and at 1604 cm^{-1} in the Raman profile of GNS-D1. Similarly, the Raman band of D1 located at 1440 cm^{-1}, which corresponds to R, underwent an important wavenumber shift toward 1472 cm^{-1} in the GNS-D1 spectrum. Based on the expression of R and Q, it is reasonable to determine that the *qshyrh* sequence has an important role in the interaction with the GNS surface. In contrast to the structural behavior of GNS-D1, a different Raman spectrum was observed in the system composed of D1 peptide linked on a GNPr surface (Fig. 5a-iii), in which Y, H, R, S, and A were identified in the profile. The presence of the characteristic bands with particular relative intensities of amino acids that constitute the complete sequence of D1 indicates that the peptide was placed plane-parallel to the GNPr surface (Fig. 5b, left); however, the orientation of a functional group of each amino acid must be perpendicular or tilted toward the surface according to the SERS selection rules (Moskovits, 1985). As can be seen from Fig. 5, the bands at 1442, 840 and 643 cm^{-1} that are attributed to R, Y/A

and Y in the Raman profile of D1, respectively, appeared at 1450, 839 and 640 cm^{-1} in the spectrum of GNPr-D1. These slight wavenumber shifts in the signals of R, Y/A and Y indicates that the conformation adopted by D1 functionalized to GNPr was quite similar to the conformation of D1 without any nanostructured surface in the proximities. Finally, the fluorescence background observed in the entire Raman profile of GNPr-D1 system indicates that the D1 peptide was more proximal to the gold surface of GNPr than to the GNS surface, resulting in fluorescence augmentation of Y and H. The fluorescence phenomenon occurred due to a formation of molecular space between the metal surface and the analyte in the presence of a capping agent, which enhanced the emission signal formed by the plasmonic effect of the nanoparticle. This plane-parallel disposition of D1 peptide over GNPr surface might block the active carboxyl groups during the functionalization process, avoiding a higher degree of conjugation and explaining the difference in the number of D1 peptide molecules between GNPr-D1 and GNS-D1. In summary, except the differences found in the number of peptide molecules per nanoparticle and their disposition over the surface, the final nanosystems present similar hydrodynamic diameters, Z.P. values, and surface areas, which makes them comparable.

3.6 Stability

Prior to the bioassays, GNPr-D1 and GNS-D1 were tested for their stability. The plasmonic bands, hydrodynamic diameters, and the Z.P. values were measured during a period of 28 days. Fig. S2 shows that both systems were stable during the whole period of study. GNPr-D1 showed some decline in the absorbance of the NIR plasmon band on day 14 and 28, but no changes were monitored in the maximum wavelength (920 nm). The hydrodynamic diameter and the Z.P. did not change significantly, starting from values of 108 nm and -24 mV and ending at 109 nm and -20 mV on day 28. Likewise, GNS-D1 showed no changes in the wavelength and the absorbance of their plasmonic band (534 nm), as well as in the Z.P. value (-32 mV). However, the hydrodynamic diameter slightly increased from 96 to 103 nm. The stability of GNPr-D1 and GNS-D1 dispersions was also evaluated in three media: milli-Q water, PBS, and RPMI medium at 37°C during a period of 24 h. Fig. S3 shows that both NP systems were stable in milli-Q water after 24 h at 37°C, with no differences in their parameters, but a decline in the absorbance of their plasmon was observed in PBS or RPMI, and especially when GNPr-D1 had been incubated in PBS. In both PBS and RPMI medium, the hydrodynamic diameter of GNPr-D1 and GNS-D1 remained constant. The Z.P. of nanoparticles incubated in PBS increased by 10 and 15 mV for GNPr-D1 and GNS-D1, respectively, while no changes were observed in RPMI medium during time. As noted, the reduction in the NIR plasmon band absorbance without changes in the plasmon band wavelength was particularly observed in samples containing GNPr-D1. It may be explained by a tendency of GNPr to interact with the plastic centrifuge tubes, which might be intensified when samples are undergone processes such as centrifugation, increasing temperature (even to 37°C), or changing the ionic strength of the medium (e.g., PBS). It is interesting to note that even using centrifuge tubes that are usually considered and claimed to be inert (e.g., Eppendorf LoBind®), a grey layer of GNPr was accumulated on the walls even after several minutes of sonication. When GNS-D1 were dispersed in PBS or RPMI, a significantly lower decrease in the plasmon absorbance was observed after incubation compared to GNPr-D1.

The colloidal stability can also be influenced by the degree of functionalization and by the type of orientation of the bound peptides. The steric repulsion or attraction between the molecules functionalized on the gold surface may result in various collisions and interaction that increase or decrease the stability of the nanoparticles, as previously described (Olmedo et al., 2008). As mentioned above, GNPr-D1 had less peptide molecules per nanoparticle compared to GNS-D1 (1300 vs. 4800, section 3.5), and the orientation and proximity of the peptides on the nanoparticles' surface were different. While the peptide was completely parallel onto the surface of GNPr, it was protruded on GNS surface by an interaction of only one edge of the sequence (*qshyrh*) with the gold surface. The lower disposition of the peptide on GNPr as well as its major proximity to the surface compared to GNS-D1 may be the reason why GNPr-D1 were relatively less stable under these specific conditions.

3.7 Cell viability

The evaluation of the effect of nanotechnology-based systems on cell viability *in vitro* has been an essential step in assessing cell penetrability and toxicity of nanoparticles. The effect of GNPr-D1 and GPS-D1 on cell viability were evaluated at various gold concentrations. The molar extinction coefficients for GNPr-D1 and GNS-D1 were determined from the plasmon-bands absorbance measurements and the particle concentrations (as determined by NTA, Fig. S4). The values obtained by linear regression were 8.6 $nM^{-1}cm^{-1}$ and 10.8 $nM^{-1}cm^{-1}$ for gold nanoprisms and gold nanospheres, respectively.

BV-2 cells have been widely used due to their suitability as an *in vitro* model of primary microglia cultures used for studying the inflammatory and toxic effects of drugs and dosage forms, as well as of nanoparticles designed for neurodegenerative disorders, such as Alzheimer and Parkinson's diseases (Duffy et al., 2016; Mrvová et al., 2015; Stojiljkovic et al., 2016; Xue et al., 2019). BV-2 cells were derived from raf/myc-immortalized murine neonatal microglia and are the most frequently used substitute for primary microglia (Henn et al., 2009; Stansley et al., 2012). A culture of microglial cell line BV-2 was incubated 24 h with GNPr-D1 or GNS-D1 at concentrations ranged from 0.05 to 1 nM and analyzed by XTT assay for cell viability (Fig. 6). XTT assay evaluates cell proliferation in cell cultures via measurement of formazan dye, a colorimetric compound that is produced enzymatically in a living cell's mitochondria (Riss et al., 2004). As presented in Fig. 6, GNPr-D1 had no effect on cell proliferation at this range of concentrations, while a gradual decline in viability was observed at elevated concentrations of GNS-D1. Below a concentration of 1 nM, the inhibition of the proliferation was not statistically significant, and only at 1 nM the proliferation was significantly inhibited ($p < 0.05$, Kruskal-Wallis test). Similar results have been published, where cytotoxic effects of different shapes of GNP (spheres, rods, and urchins) in a culture of microglia cell line N9 were evaluated (Hutter et al., 2010). This report showed that GNS functionalized with PEG were significantly cytotoxic at concentrations $\geq 10^9$ NP/mL (0.017 nM approximately), whereas the gold nanorods and urchins were innocuous. It is well known that the shape of the nanoparticle (and not just its size) influences cellular penetration and accumulation, which may trigger the inhibition of cellular proliferation through different mechanisms that do not necessarily involve cellular death, as previously studied in BV-2 cells (Gusain et al., 2012; Mrvová et al., 2015). Another report that compared the cell internalization of spheres and rods (Chithrani and Chan, 2007) has shown that

spheres accumulated at higher proportions compared to rods. One explanation is that nanoparticles with an aniosotropic shape can interact with the cell membrane through different axis. If this interaction occurs through the longitudinal axis of gold nanorods, the contact area that covers the membrane is larger compared to the area covered by gold nanospheres, and limits the cellular surface available for the internalization process. A similar scenario could happen when GNPr-D1 interacts with the cell surface through their triangular faces, limiting their cellular penetration compared with GNS-D1 interaction. Furthermore, the mean diameter of GNS-D1 was 47 nm, which is an optimal size for membranal penetration as previously determined (Chithrani et al., 2006). This publication [37] has demonstrated a higher cellular uptake of gold nanospheres with 50 nm in diameter compared with various nanospheres at different sizes. Understanding of the mechanism by which nanoparticles penetrate across cell membrane and internalize into the cells has remained to be explored.

3.8 IN administration

3.8.1 Comparison between GNPr-D1 and GNS-D1

The general goal of this research was to test the ability of gold nanoparticles to be trafficked into the brain via the 'nose-to-brain' route. Sprague-Dawley rats were grouped and administered with GNPr-D1 or GNS-D1 ($4.5x10^{11}$ nanoparticles/kg of body weight). Brain and olfactory bulb were removed separately, and blood samples were taken by cardiac puncture. All samples were digested, and the amount of gold was determined by ICP-MS (Fig. 7). Fig. 7a shows that major quantities of gold were found in the brain after IN administration of GNS-D1. There was a significant difference between the amount of gold found in the brain after GNPr-D1 (0.54 ± 0.08 ng Au/g tissue) and GNS-D1 (3.01 ± 0.84 ng Au/g tissue) ($p<0.05$). GNS-D1 also penetrated at high levels into the olfactory bulbs, supporting the general statement that they are considered as the open gate to the brain. In the olfactory bulbs, GNPr-D1 was accumulated at a lower average concentration relative to GNS-D1, i.e., 12.80 ± 3.02 vs. 67.69 ± 48.95 ng Au/g tissue (Fig. 7b). Similarly, GNS-D1 presented a higher absorption into the systemic circulation reaching a mean plasma level of 1.45 ± 0.78 ng Au/mL as compared to GRPr-D1, which reached only 0.78 ± 0.29 ng Au/mL (Fig. 7c). Nevertheless, and unlike brain levels, the differences between the levels found in the olfactory bulbs and plasma were not statistically significant.

There are currently a few studies dealing with 'nose-to-brain' delivery of metal nanoparticles. Most studies associated with CNS exposure to metal nanoparticles have been focused on the neuronal toxicity as a result of environmental pollution of metals rather than on neurological therapeutics or diagnostics (Elder et al., 2006; Liu et al., 2014; Wu et al., 2013; Yin et al., 2015a; Yin et al., 2015b; Ze et al., 2013). The first study with GNP, published 50 years ago, reported that gold was detected in the cerebro-spinal fluid of the anterior cranial fossa after a colloidal ^{198}Au was applied to the mucosa of the olfactory region in rabbits (Czerniawska, 1970). To this date, the exact mechanism involved in the direct transport of nanoparticles from nose to brain is still not completely understood, and only two pathways that innervate the epithelium of the nasal cavity have been described. The two pathways are the olfactory nerve and the trigeminal nerve, which enter into the brain through the olfactory bulb and pons, respectively (Lochhead and Thorne, 2012). Hutter et al., 2010 studied the effect of the morphology of gold nanoparticles (spheres, rods, and urchins - coated with PEG or

CTAB) on the brain by evaluating the microglial response after IN administration. The transgenic mouse model was used to evaluate the transient toll-like receptor 2 (TLR-2) upregulation in the olfactory bulb after IN administration. The results have shown that the morphology and the surface chemistry influenced the microglial activation. Although they did not evaluate the amount of gold that reached the CNS, *in vitro* experiments revealed that the extent of internalization for anisotropic shape, especially for urchins, was greater compared to spheres, and the researchers, therefore, suggested that nanourchins were preferentially taken up by microglial cells rather than by the neurons. These previous results are apparently in contrast to the results presented in the present report. Although nanoprisms is different from nanourchins, the *in vitro* data suggested that nanospheres did internalize cells to a greater extent than nanoprisms. Taking this into consideration, we reasonably hypothesize that a similar scenario may occur when the nanosystems were intranasally administered, namely, GNS-D1 would penetrate cells in a higher ratio than GNPr-D1, facilitating their translocation from the nasal cavity to the CNS (brain and olfactory bulb) and to systemic circulation (plasma). In addition to the olfactory bulb, gold nanoparticles can be transported through the trigeminal nerve. A recent study evaluated the nose-to-brain delivery of gold nanoclusters with a hydrodynamic size of approximately 6 nm after administration to C57BL/6 female mice (Ye et al., 2018). By using a focused ultrasound radiation combined with microbubbles (FUSIN), they have shown that nanoclusters were present in trigeminal nerve and reached the CNS after IN administration and the delivery was enhanced by FUSIN. However, since the researchers measured radioactivity and fluorescence intensity instead of direct quantification of gold (by ICP-MS for instance), and since isolation of the trigeminal nerve was beyond the scope of this paper, the extent of GNS-D1 and GNPr-D1 delivery through the trigeminal nerve could not be estimated in this study, and should be further explored.

The difference that was observed between the brain uptakes of GNS-D1 and GNPr-D1 after IN administration may be explained by the difference in their way of interaction with cell membranes. Another explanation might be a difference in their absorption from the nasal cavity into the systemic circulation, and thereby through the BBB to brain (the indirect systemic route). However, although we cannot completely discard this process, it seems unlikely. First, no significant difference in gold levels were monitored in plasma after 0.5 h, and secondly, neither GNS-D1 nor GNPr-D1 has a recognizable transporter or known to have a physicochemical feature (such as hydrophobicity), which would facilitate their passage through the BBB. Due to the higher amount of gold found in the CNS after GNS-D1 administration compared to GNPr-D1 administration, further pharmacokinetic experiments were set up with GNS-D1 only.

3.8.2 Pharmacokinetic study of GNS-D1 after IN administration

Since bioaccumulation of GNS-D1 in the brain after IN administration was the main goal of this study, it was important to determine when this specific nanosystem would reach a peak level in the CNS (t_{max}), and when it would be eliminated from plasma and from various body organs. To evaluate this, a pharmacokinetic study was carried out in rats (Fig. 8). The animals were sacrificed after 0.75, 2, 4, 8, and 24 h following IN administration of GNS-D1 (n=3 for each time group). The perfused organs were lyophilized, triturated, and homogenized. Samples were analyzed by neutron activation to determine the amount of gold, which is relatively more sensitive than ICP-MS analysis. Fig. 8a-d

shows the obtained gold levels in brain, olfactory bulb, plasma, and liver versus time for a period of 24h. The highest concentrations of gold were found at 0.75 h in the brain, olfactory bulb, and plasma after IN administration. These concentrations were significantly higher than those presented in Fig. 7, which were determined after 0.5 h from GNS-D1 administration, so they are considered as peak levels (C_{max}), although the precise peak might be between the range of 30-45min. During this 15 min interval, the gold level in the brain increased 35-fold to 106 ± 19 ng Au/g tissue, whereas in the olfactory bulb and plasma it increased by 3- and 15-fold (175 ± 55 ng Au/g tissue and 21 ± 4 ng Au/mL), respectively. From 0.75h to 2h after administration, a fast elimination phase was noted in brain, olfactory bulb and plasma. The gold elimination in the brain was followed by an additional lower uptake rate of gold that remained constant up to 24 h. Unlike the small elevation of gold in the brain, a second peak was observed 8 h after the administration in both olfactory bulb and plasma, which was declined to a relatively low levels at 24 h. In the liver, however, gold levels were slowly elevated during 8 hours and then a faster accumulation of the gold was observed from 8h to 24 h, a 100-fold increase that reached a value of 450 ± 370 ng Au/g of tissue.

The data indicates that the translocation of nanoparticles to the brain after IN administration occurred in two peaks - the first one is characterized by a great "burden" of GNS-D1 reaching the brain during a short period of time (45 min), followed by a slow nanoparticle absorption resulting in low uptake levels of gold. This interesting phenomenon may be explained by: (1) two possible mechanisms having different CNS penetrability or existence of two different anatomical routes for 'nose-to-brain' delivery of gold nanoparticles (one faster than the other), and (2) direct delivery of nose-to-brain delivery followed by an indirect systemic transport of gold nanoparticles via the BBB into brain tissue. An associated example for the second explanation can be the IN administration of sumatriptan, which exhibited a two-peak pharmacokinetic behavior of systemic absorption (Djupesland et al., 2013). Sumatriptan is a selective agonist acting on vascular 5-hydroxytryptamine (5-HT1B/1D) receptors, used for treatment of migraine attacks. It has been found that a more pronounced early peak represents direct nasal absorption, and a reduced late peak represents predominantly an indirect gastrointestinal (GI) absorption.

3.8.3 Comparison between IN and IV administration of GNS-D1

The measure of absorption of IN gold nanoparticles into the systemic circulation and from the blood into the brain through the BBB (the indirect route), can be estimated by IV bolus administration. Both IN and IV routes were compared at 0.75 h, which has considered to be the peak brain level after the nasal application (Fig. 9). The brain, plasma and other organs (olfactory bulb, liver, spleen, lungs) were analyzed for gold exposure. The levels of gold found in the brain, olfactory bulb, and plasma were significantly greater after IN administration compared to IV administration. A concentration of 106 ± 19 ng Au/g tissue were found in the brain after IN administration while only 1.9 ± 0.9 ng Au/g tissue were found after IV injection ($p < 0.01$). Similarly, 175 ± 55 ng Au/g tissue were analyzed in the olfactory bulbs after 45min following IN administration compared to only 7 ± 5 ng Au/g tissue after IV injection ($p < 0.05$). The elimination rate of the gold nanoparticles in the plasma was indicated by a significant elevation of gold in the liver after IV administration, i.e., 2500 ± 950 ng Au/g tissue, whereas only 1.7 ± 0.6 ng Au/g tissue were detected in the liver after nasal administration. Similar difference in gold levels were found in the spleen, i.e., 2300 ± 770 ng Au/g

tissue (IV) and 2.2± 0.7 ng Au/g tissue (IN). Very small amounts of gold reached the lungs after both administrations, where the difference between them was 30 ± 16 ng Au/g tissue (IV) and 0.9 ± 0.4 ng Au/g tissue (IN) (Fig. 9). The gold levels in the plasma after IN administration were significantly higher than those obtained after IV administration, i.e., 21 ± 5 ng Au/mL (IN) and 0.7 ± 0.4 ng Au/mL (IV) ($p < 0.05$), indicating that gold nanoparticles were cleared from the brain and the nasal cavity into the blood. Since the elimination from these depot sites has occurred in a timed-release manner, it can explain the lower levels of gold found in the liver after IN administration in comparison to the IV bolus. The higher levels observed in brain by the IN route could be explained mainly by two phenomena: bypassing the BBB allows a direct transport of GNS-D1 from the nasal cavity to the brain, and reduced systemic exposure that avoid the retention by liver and spleen, which consequently reduce the bioavailability of GNS-D1. It should be pointed out that the percentage of the administered dose of gold in brain was 0.05% (IN) compared to 0.001% (IV) (see Fig. S5), which is similar to previous reports (Guerrero et al., 2010; Velasco-Aguirre et al., 2017). However, the percentages of the dose in the liver and the spleen were extremely lower compared to these reports, 80% vs 0.01% and 15% vs 0.001%, respectively. It was also notable that the maximal level of gold found in liver after 24h was only 2%, (Fig. 8d). These results clearly show that by using the IN route rather than the IV route, a fast and significant delivery of gold nanoparticles to the CNS is obtained while avoiding systemic exposure and possible adverse effects.

3.8.4 Brain distribution of GNS-D1 after IN and IV administration

The difference in the total uptake of gold in the brain between IN and IV administrations is interesting by itself but it does not provide an information as to the way gold is distributed relative to the route of its delivery. It had been obviously hypothesized that the IN route would result in a concentration gradient from the olfactory region along the cerebellum, while more uniform distribution would be observed after IV administration. To determine the distribution of GNS-D1 in brain and olfactory bulb, rats were administered intranasally and intravenously with the same dose of GNS-D1, and the brain was extracted after 0.75 h, sectioned (coronary plane) and analyzed for gold by visibility enhancement as described in the experimental section. Fig. 10 shows the localization of GNS-D1 in different brain cuts, from the olfactory bulb to the cerebellum (a detailed list of data can be found in Table S2). The results show that there was generally not much difference in biodistribution of gold between the IN and IV routes, except the olfactory bulbs. These distribution results are apparently in contrast to the quantitative results, a phenomenon that has also been reported (Talamini et al., 2017). The difference between the qualitative and the quantitative methods may be explained by fast accumulation and creation of gold clusters inside the parenchyma cells after IN administration, while IV injected GNS (already covered by protein corona) cannot create clusters and distribute between the cells, thus developing more intense staining.

Finally, we calculated the percentage of gold loci for each region. It was revealed that a greater percentage of GNS-D1 was observed in the basal forebrain, thalamus, and cerebellum after IV injection rather than after IN administration, whereas a major percentage of the nanoparticles after IN administration was observed in the periaqueductal gray, perirhinal and entorhinal cortex, olfactory bulb, and hippocampus region. Neocortex region showed the highest percentage of gold

after either IN or IV administration, with values of 28% and 34%, respectively. It should be pointed out that the results of brain distribution of gold were specific for t_{max} only (0.75 h), when the concentration of gold nanoparticles in the brain after IN administration is at maximum. Future experiments should be designed to study the distribution pattern in time course, using more advanced technologies, such as computed tomography. A recent publication has described a technique for *in vivo* neuroimaging of exosomes labeled with gold nanoparticles which were IN administered to C57BL/6 male mice (Betzer et al., 2017). The researchers detected a sustained quantity of labeled exosomes in the stroke region of the brain by ICP-MS and computed tomography up to 24 h after IN administration.

The therapeutics and/or diagnostic efficacy of GNP are dependent on the ability of the nanoparticles to target a specific site where the disease is developing. The brain biodistribution analysis done by the gold visibility enhancement has shown that GNS-D1 is located in the cortex and hippocampus areas, which are the sites in brain where accumulation of Aβ plaques occurs. These zones have been widely studied in transgenic murine models for Alzheimer disease (Cohen et al., 2013; Garcia-Alloza et al., 2006; Jackson et al., 2016; Jankowsky et al., 2004). In a future research, nose-to-brain delivery of GNS-D1 should be studied in a transgenic model for Alzheimer disease (e.g. APP mouse), tracing the preferential localizations of the nanoparticles in brain areas where $A\beta_{1-42}$ accumulates. It is presumed that site localization in Alzheimer disease may be achieved due to the interaction between D1 peptide on the surface of the nanoparticles with the toxic aggregates that typify the disease.

4. Conclusions

The present research has further clarified the advantages of the IN route in targeting nanosystems to the CNS for the treatment and/or diagnosis of different pathologies, such as Alzheimer Disease and parkinsonism. In this study we have developed two new nanosystem based on GNPr or GNS functionalized with PEG and D1, and demonstrated that both were stable in different conditions and did not affect BV-2 cell viability for concentrations ranging from 0.05 to 0.5 nM. IN administration revealed that despite both nanosystems had similar features such as surface area, hydrodynamic diameter, and surface charge, their different shape significantly influenced their translocation from the nasal cavity to the brain, being greater for nanospheres (GNS-D1). The use of other nanomaterials and shapes may help in the understanding of how different physicochemical features affect the uptake of nanomaterials from the nose to CNS. Data obtained from a pharmacokinetic study with GNS-D1 indicated that the translocation of nanoparticles from nasal cavity to the brain occurs in two phases, which may be attributed to the existence of two mechanisms of transportation, or the presence of both direct/indirect transport. Future mechanistic studies that address the IN route of delivery are important and necessary to comprehend the mechanisms involved in nose-to-brain transport. Through the comparison of IN and IV administration of GNS-D1, we obtained results that strongly support the use of IN administration as a promising route for drug and GNP delivery to the CNS, while avoiding systemic exposure. More studies with transgenic models should be carried out to evaluate the accumulation of the newly developed nanosystem in Aβ plaques, and to elucidate the feasibility of using GNP for neurodegenerative diseases.

Acknowledgments

The authors thank Pedro Jara-Guajardo (PhD student, Departamento de Química Farmacológica y Toxicológica, Facultad de Ciencias Químicas y Farmacéuticas, Universidad de Chile, Chile), Carolina Velasco-Aguirre (PhD), and the staff of Ilze Katz Institute for Nanoscale Science & Technology (Ben-Gurion University of the Negev, Be'er Sheva, Israel) for their technical support. Eyleen Araya (PhD, Departamento de Ciencias Químicas, Facultad de Ciencias Exactas, Universidad Andres Bello, Chile) and Fernando Albericio (PhD, University of KwaZulu-Natal, South Africa) for D1 peptide.

Funding

This work was supported by ANID, Ministry of Science, Chile [PhD fellowship number 21151400]; project FONDECYT [number 1170929]; and project FONDAP [number 15130011].

Declaration of Competing Interest

The authors declare no conflict of interest.

Authors contributions

E.G. performed most of the experiments, drafted the manuscript, and prepared figures. A.T. contributed to the synthesis, purification, and functionalization of GNPr and the discussion of the results. F.C. conducted Raman spectroscopy experiments to determine the disposition of D1 peptide over the gold surface and wrote down the corresponding section in the manuscript. T.S. carried out the cell proliferation assays in BV-2 cells. M.C. directed Raman spectroscopy analysis and facilitated the equipment. M.K. and A.S. directed the thesis research, planned the manuscript, and helped write down and edit the manuscript and figures. A.S. performed administrations for most of the *in vivo* experiments.

References

Adura, C., Guerrero, S., Salas, E., Medel, L., Riveros, A., Mena, J., Arbiol, J., Albericio, F., Giralt, E., Kogan, M.J., 2013. Stable Conjugates of Peptides with Gold Nanorods for Biomedical Applications with Reduced Effects on Cell Viability. Acs Appl Mater Inter 5, 4076-4085.

Alalaiwe, A., 2019. The clinical pharmacokinetics impact of medical nanometals on drug delivery system. Nanomedicine 17, 47-61.

Aliaga, A.E., Aguayo, T., Garrido, C., Clavijo, E., Hevia, E., Gomez-Jeria, J.S., Leyton, P., Campos-Vallette, M.M., Sanchez-Cortes, S., 2011. Surface-enhanced Raman scattering and theoretical studies of the C-terminal peptide of the beta-subunit human chorionic gonadotropin without linked carbohydrates. Biopolymers 95, 135-143.

Aliaga, A.E., Garrido, C., Leyton, P., Diaz, G., Gomez-Jeria, J.S., Aguayo, T., Clavijo, E., Campos-Vallette, M.M., Sanchez-Cortes, S., 2010. SERS and theoretical studies of arginine. Spectrochimica acta. Part A, Molecular and biomolecular spectroscopy 76, 458-463.

Arvizo, R.R., Giri, K., Moyano, D., Miranda, O.R., Madden, B., McCormick, D.J., Bhattacharya, R., Rotello, V.M., Kocher, J.P., Mukherjee, P., 2012. Identifying New Therapeutic Targets via Modulation of Protein Corona Formation by Engineered Nanoparticles. PloS one 7.

Bergen, J.M., von Recum, H.A., Goodman, T.T., Massey, A.P., Pun, S.H., 2006. Gold nanoparticles as a versatile platform for optimizing physicochemical parameters for targeted drug delivery. Macromolecular bioscience 6, 506-516.

Betzer, O., Perets, N., Angel, A., Motiei, M., Sadan, T., Yadid, G., Offen, D., Popovtzer, R., 2017. In Vivo Neuroimaging of Exosomes Using Gold Nanoparticles. ACS nano 11, 10883-10893.

Cauda, V., Argyo, C., Bein, T., 2010. Impact of different PEGylation patterns on the long-term bio-stability of colloidal mesoporous silica nanoparticles. Journal of Materials Chemistry 20, 8693-8699.

Cohen, R.M., Rezai-Zadeh, K., Weitz, T.M., Rentsendorj, A., Gate, D., Spivak, I., Bholat, Y., Vasilevko, V., Glabe, C.G., Breunig, J.J., Rakic, P., Davtyan, H., Agadjanyan, M.G., Kepe, V., Barrio, J.R., Bannykh, S., Szekely, C.A., Pechnick, R.N., Town, T., 2013. A transgenic Alzheimer rat with plaques, tau pathology, behavioral impairment, oligomeric abeta, and frank neuronal loss. The Journal of neuroscience : the official journal of the Society for Neuroscience 33, 6245-6256.

Culka, A., Jehlicka, J., Edwards, H.G., 2010. Acquisition of Raman spectra of amino acids using portable instruments: outdoor measurements and comparison. Spectrochimica acta. Part A, Molecular and biomolecular spectroscopy 77, 978-983.

Czerniawska, A., 1970. Experimental investigations on the penetration of 198Au from nasal mucous membrane into cerebrospinal fluid. Acta oto-laryngologica 70, 58-61.

Chithrani, B.D., Chan, W.C., 2007. Elucidating the mechanism of cellular uptake and removal of protein-coated gold nanoparticles of different sizes and shapes. Nano letters 7, 1542-1550.

Chithrani, B.D., Ghazani, A.A., Chan, W.C., 2006. Determining the size and shape dependence of gold nanoparticle uptake into mammalian cells. Nano letters 6, 662-668.

Dell'Orco, D., Lundqvist, M., Oslakovic, C., Cedervall, T., Linse, S., 2010. Modeling the time evolution of the nanoparticle-protein corona in a body fluid. PloS one 5, e10949.

Dhuria, S.V., Hanson, L.R., Frey, W.H., 2nd, 2010. Intranasal delivery to the central nervous system: mechanisms and experimental considerations. Journal of pharmaceutical sciences 99, 1654-1673.

Djupesland, P.G., Messina, J.C., Mahmoud, R.A., 2013. Breath powered nasal delivery: a new route to rapid headache relief. Headache 53 Suppl 2, 72-84.

Duffy, C.M., Ahmed, S., Yuan, C., Mavanji, V., Nixon, J.P., Butterick, T., 2016. Microglia as a Surrogate Biosensor to Determine Nanoparticle Neurotoxicity. Journal of visualized experiments : JoVE.

El-Sayed, I.H., Huang, X., El-Sayed, M.A., 2005. Surface plasmon resonance scattering and absorption of anti-EGFR antibody conjugated gold nanoparticles in cancer diagnostics: applications in oral cancer. Nano letters 5, 829-834.

Elder, A., Gelein, R., Silva, V., Feikert, T., Opanashuk, L., Carter, J., Potter, R., Maynard, A., Ito, Y., Finkelstein, J., Oberdorster, G., 2006. Translocation of inhaled ultrafine manganese oxide particles to the central nervous system. Environmental health perspectives 114, 1172-1178.

Findeis, M.A., Musso, G.M., Arico-Muendel, C.C., Benjamin, H.W., Hundal, A.M., Lee, J.J., Chin, J., Kelley, M., Wakefield, J., Hayward, N.J., Molineaux, S.M., 1999. Modified-peptide inhibitors of amyloid beta-peptide polymerization. Biochemistry 38, 6791-6800.

Frigell, J., Garcia, I., Gomez-Vallejo, V., Llop, J., Penades, S., 2014. 68Ga-labeled gold glyconanoparticles for exploring blood-brain barrier permeability: preparation, biodistribution studies, and improved brain uptake via neuropeptide conjugation. J Am Chem Soc 136, 449-457.

Gao, H., 2016. Progress and perspectives on targeting nanoparticles for brain drug delivery. Acta pharmaceutica Sinica. B 6, 268-286.

Garcia-Alloza, M., Robbins, E.M., Zhang-Nunes, S.X., Purcell, S.M., Betensky, R.A., Raju, S., Prada, C., Greenberg, S.M., Bacskai, B.J., Frosch, M.P., 2006. Characterization of amyloid deposition in the APPswe/PS1dE9 mouse model of Alzheimer disease. Neurobiology of disease 24, 516-524.

Garrido, C., Aliaga, A.E., Gomez-Jeria, J.S., Carcamo, J.J., Clavijo, E., Campos-Vallette, M.M., 2012. Interaction of the C-terminal peptide from pigeon cytochrome C with silver nanoparticles. A Raman, SERS and theoretical study. Vib Spectrosc 61, 94-98.

Ghosh, P., Han, G., De, M., Kim, C.K., Rotello, V.M., 2008. Gold nanoparticles in delivery applications. Advanced drug delivery reviews 60, 1307-1315.

Guerrero, S., Araya, E., Fiedler, J.L., Arias, J.I., Adura, C., Albericio, F., Giralt, E., Arias, J.L., Fernandez, M.S., Kogan, M.J., 2010. Improving the brain delivery of gold nanoparticles by conjugation with an amphipathic peptide. Nanomedicine 5, 897-913.

Guerrero, S., Herance, J.R., Rojas, S., Mena, J.F., Gispert, J.D., Acosta, G.A., Albericio, F., Kogan, M.J., 2012. Synthesis and in vivo evaluation of the biodistribution of a 18F-labeled conjugate gold-nanoparticle-peptide with potential biomedical application. Bioconjugate chemistry 23, 399-408.

Gusain, A., Hatcher, J.F., Adibhatla, R.M., Wesley, U.V., Dempsey, R.J., 2012. Anti-proliferative Effects of Tricyclodecan-9-yl-xanthogenate (D609) Involve Ceramide and Cell Cycle Inhibition. Molecular Neurobiology 45, 455-464.

Henn, A., Lund, S., Hedtjarn, M., Schrattenholz, A., Porzgen, P., Leist, M., 2009. The suitability of BV2 cells as alternative model system for primary microglia cultures or for animal experiments examining brain inflammation. Altex 26, 83-94.

Hetenyi, C., Kortvelyesi, T., Penke, B., 2002. Mapping of possible binding sequences of two beta-sheet breaker peptides on beta amyloid peptide of Alzheimer's disease. Bioorgan Med Chem 10, 1587-1593.

Huang, X., Peng, X., Wang, Y., Wang, Y., Shin, D.M., El-Sayed, M.A., Nie, S., 2010. A reexamination of active and passive tumor targeting by using rod-shaped gold nanocrystals and covalently conjugated peptide ligands. ACS nano 4, 5887-5896.

Hutter, E., Boridy, S., Labrecque, S., Lalancette-Hebert, M., Kriz, J., Winnik, F.M., Maysinger, D., 2010. Microglial response to gold nanoparticles. ACS nano 4, 2595-2606.

Illum, L., 2000. Transport of drugs from the nasal cavity to the central nervous system. European journal of pharmaceutical sciences : official journal of the European Federation for Pharmaceutical Sciences 11, 1-18.

Illum, L., 2002. Nasal drug delivery: new developments and strategies. Drug discovery today 7, 1184-1189.

Illum, L., 2003. Nasal drug delivery--possibilities, problems and solutions. Journal of controlled release : official journal of the Controlled Release Society 87, 187-198.

Illum, L., 2004. Is nose-to-brain transport of drugs in man a reality? J Pharm Pharmacol 56, 3-17.

Iyer, A.K., Khaled, G., Fang, J., Maeda, H., 2006. Exploiting the enhanced permeability and retention effect for tumor targeting. Drug discovery today 11, 812-818.

Jackson, R.J., Rudinskiy, N., Herrmann, A.G., Croft, S., Kim, J.M., Petrova, V., Ramos-Rodriguez, J.J., Pitstick, R., Wegmann, S., Garcia-Alloza, M., Carlson, G.A., Hyman, B.T., Spires-Jones, T.L., 2016. Human tau increases amyloid beta plaque size but not amyloid beta-mediated synapse loss in a novel mouse model of Alzheimer's disease. The European journal of neuroscience 44, 3056-3066.

Jain, P.K., Huang, X., El-Sayed, I.H., El-Sayed, M.A., 2008. Noble metals on the nanoscale: optical and photothermal properties and some applications in imaging, sensing, biology, and medicine. Accounts of chemical research 41, 1578-1586.

Jankowsky, J.L., Fadale, D.J., Anderson, J., Xu, G.M., Gonzales, V., Jenkins, N.A., Copeland, N.G., Lee, M.K., Younkin, L.H., Wagner, S.L., Younkin, S.G., Borchelt, D.R., 2004. Mutant presenilins specifically elevate the levels of the 42 residue beta-amyloid peptide in vivo: evidence for augmentation of a 42-specific gamma secretase. Human molecular genetics 13, 159-170.

Karhanek, M., Kemp, J.T., Pourmand, N., Davis, R.W., Webb, C.D., 2005. Single DNA molecule detection using nanopipettes and nanoparticles. Nano letters 5, 403-407.

Kjonigsen, L.J., Lillehaug, S., Bjaalie, J.G., Witter, M.P., Leergaard, T.B., 2015. Waxholm Space atlas of the rat brain hippocampal region: three-dimensional delineations based on magnetic resonance and diffusion tensor imaging. NeuroImage 108, 441-449.

Kogan, M.J., Bastus, N.G., Amigo, R., Grillo-Bosch, D., Araya, E., Turiel, A., Labarta, A., Giralt, E., Puntes, V.F., 2006. Nanoparticle-mediated local and remote manipulation of protein aggregation. Nano letters 6, 110-115.

Kohler, N., Sun, C., Wang, J., Zhang, M., 2005. Methotrexate-modified superparamagnetic nanoparticles and their intracellular uptake into human cancer cells. Langmuir : the ACS journal of surfaces and colloids 21, 8858-8864.

Liu, H., Funke, S.A., Willbold, D., 2010. Transport of Alzheimer disease amyloid-beta-binding D-amino acid peptides across an in vitro blood-brain barrier model. Rejuvenation research 13, 210-213.

Liu, T., Shi, S., Liang, C., Shen, S., Cheng, L., Wang, C., Song, X., Goel, S., Barnhart, T.E., Cai, W., Liu, Z., 2015. Iron oxide decorated MoS2 nanosheets with double PEGylation for chelator-free radiolabeling and multimodal imaging guided photothermal therapy. ACS nano 9, 950-960.

Liu, Y., Gao, Y., Liu, Y., Li, B., Chen, C., Wu, G., 2014. Oxidative stress and acute changes in murine brain tissues after nasal instillation of copper particles with different sizes. Journal of nanoscience and nanotechnology 14, 4534-4540.

Lochhead, J.J., Thorne, R.G., 2012. Intranasal delivery of biologics to the central nervous system. Advanced drug delivery reviews 64, 614-628.

Long, D.A., 2004. Infrared and Raman characteristic group frequencies. Tables and charts George Socrates John Wiley and Sons, Ltd, Chichester, Third Edition, 2001. Price £135. Journal of Raman Spectroscopy 35, 905-905.

Lundqvist, M., Stigler, J., Elia, G., Lynch, I., Cedervall, T., Dawson, K.A., 2008. Nanoparticle size and surface properties determine the protein corona with possible implications for biological impacts. Proceedings of the National Academy of Sciences of the United States of America 105, 14265-14270.

Millstone, J.E., Park, S., Shuford, K.L., Qin, L., Schatz, G.C., Mirkin, C.A., 2005. Observation of a quadrupole plasmon mode for a colloidal solution of gold nanoprisms. Journal of the American Chemical Society 127, 5312-5313.

Monopoli, M.P., Walczyk, D., Campbell, A., Elia, G., Lynch, I., Bombelli, F.B., Dawson, K.A., 2011. Physical-chemical aspects of protein corona: relevance to in vitro and in vivo biological impacts of nanoparticles. J Am Chem Soc 133, 2525-2534.

Morales-Zavala, F., Arriagada, H., Hassan, N., Velasco, C., Riveros, A., Alvarez, A.R., Minniti, A.N., Rojas-Silva, X., Munoz, L.L., Vasquez, R., Rodriguez, K., Sanchez-Navarro, M., Giralt, E., Araya, E., Aldunate, R., Kogan, M.J., 2017. Peptide multifunctionalized gold nanorods decrease toxicity of beta-amyloid peptide in a Caenorhabditis elegans model of Alzheimer's disease. Nanomedicine 13, 2341-2350.

Moskovits, M., 1985. Surface-Enhanced Spectroscopy. Rev Mod Phys 57, 783-826.

Mrvová, N., Škandík, M., Kuniaková, M., Račková, L., 2015. Modulation of BV-2 microglia functions by novel quercetin pivaloyl ester. Neurochemistry International 90, 246-254.

Ng, C.T., Tang, F.M., Li, J.J., Ong, C., Yung, L.L., Bay, B.H., 2015. Clathrin-mediated endocytosis of gold nanoparticles in vitro. Anatomical record 298, 418-427.

Olmedo, I., Araya, E., Sanz, F., Medina, E., Arbiol, J., Toledo, P., Alvarez-Lueje, A., Giralt, E., Kogan, M.J., 2008. How changes in the sequence of the peptide CLPFFD-NH2 can modify the conjugation and stability of gold nanoparticles and their affinity for beta-amyloid fibrils. Bioconjugate chemistry 19, 1154-1163.

Papp, E.A., Leergaard, T.B., Calabrese, E., Johnson, G.A., Bjaalie, J.G., 2014. Waxholm Space atlas of the Sprague Dawley rat brain. NeuroImage 97, 374-386.

Pardridge, W.M., 2007. Blood-brain barrier delivery. Drug discovery today 12, 54-61.

Pelaz, B., Grazu, V., Ibarra, A., Magen, C., del Pino, P., de la Fuente, J.M., 2012. Tailoring the synthesis and heating ability of gold nanoprisms for bioapplications. Langmuir : the ACS journal of surfaces and colloids 28, 8965-8970.

Pelaz García, B., 2012. Doctoral Thesis: Tayloring the synthesis and the functionalization of nanoparticles for nanomedicine. Universidad de Zaragoza Repository. http://zaguan.unizar.es/record/7468/files/TESIS-2012-070.pdf

Prades, R., Guerrero, S., Araya, E., Molina, C., Salas, E., Zurita, E., Selva, J., Egea, G., Lopez-Iglesias, C., Teixido, M., Kogan, M.J., Giralt, E., 2012. Delivery of gold nanoparticles to the brain by conjugation with a peptide that recognizes the transferrin receptor. Biomaterials 33, 7194-7205.

Riss, T.L., Moravec, R.A., Niles, A.L., Duellman, S., Benink, H.A., Worzella, T.J., Minor, L., 2004. Cell Viability Assays, in: Sittampalam, G.S., Coussens, N.P., Brimacombe, K., Grossman, A., Arkin, M., Auld, D., Austin, C., Baell, J., Bejcek, B., Caaveiro, J.M.M., Chung, T.D.Y., Dahlin, J.L., Devanaryan, V., Foley, T.L., Glicksman, M., Hall, M.D., Haas, J.V., Inglese, J., Iversen, P.W., Kahl, S.D., Kales, S.C., Lal-Nag, M., Li, Z., McGee, J., McManus, O., Riss, T., Trask, O.J., Jr., Weidner, J.R., Wildey, M.J., Xia, M., Xu, X. (Eds.), Assay Guidance Manual, Bethesda (MD).

Salem, H.F., Kharshoum, R.M., Abou-Taleb, H.A., Naguib, D.M., 2019. Brain targeting of resveratrol through intranasal lipid vesicles labelled with gold nanoparticles: in vivo evaluation and bioaccumulation investigation using computed tomography and histopathological examination. Journal of Drug Targeting, 1-34.

Schaffler, M., Sousa, F., Wenk, A., Sitia, L., Hirn, S., Schleh, C., Haberl, N., Violatto, M., Canovi, M., Andreozzi, P., Salmona, M., Bigini, P., Kreyling, W.G., Krol, S., 2014. Blood protein coating of gold nanoparticles as potential tool for organ targeting. Biomaterials 35, 3455-3466.

Sergejeva, M., Papp, E.A., Bakker, R., Gaudnek, M.A., Okamura-Oho, Y., Boline, J., Bjaalie, J.G., Hess, A., 2015. Anatomical landmarks for registration of experimental image data to volumetric rodent brain atlasing templates. Journal of neuroscience methods 240, 161-169.

Shilo, M., Motiei, M., Hana, P., Popovtzer, R., 2014. Transport of nanoparticles through the blood-brain barrier for imaging and therapeutic applications. Nanoscale 6, 2146-2152.

Soto, C., Sigurdsson, E.M., Morelli, L., Kumar, R.A., Castano, E.M., Frangione, B., 1998. Beta-sheet breaker peptides inhibit fibrillogenesis in a rat brain model of amyloidosis: implications for Alzheimer's therapy. Nature medicine 4, 822-826.

Stansley, B., Post, J., Hensley, K., 2012. A comparative review of cell culture systems for the study of microglial biology in Alzheimer's disease. Journal of neuroinflammation 9, 115.

Steinmetz, N.F., Manchester, M., 2009. PEGylated viral nanoparticles for biomedicine: the impact of PEG chain length on VNP cell interactions in vitro and ex vivo. Biomacromolecules 10, 784-792.

Stojiljkovic, A., Kuehni-Boghenbor, K., Gaschen, V., Schupbach, G., Mevissen, M., Kinnear, C., Moller, A.M., Stoffel, M.H., 2016. High-content analysis of factors affecting gold nanoparticle uptake by neuronal and microglial cells in culture. Nanoscale 8, 16650-16661.

Talamini, L., Violatto, M.B., Cai, Q., Monopoli, M.P., Kantner, K., Krpetic, Z., Perez-Potti, A., Cookman, J., Garry, D., C, P.S., Boselli, L., Pelaz, B., Serchi, T., Cambier, S., Gutleb, A.C., Feliu, N., Yan, Y., Salmona, M., Parak, W.J., Dawson, K.A., Bigini, P., 2017. Influence of Size and Shape on the Anatomical Distribution of Endotoxin-Free Gold Nanoparticles. ACS nano 11, 5519-5529.

Tenzer, S., Docter, D., Rosfa, S., Wlodarski, A., Kuharev, J., Rekik, A., Knauer, S.K., Bantz, C., Nawroth, T., Bier, C., Sirirattanapan, J., Mann, W., Treuel, L., Zellner, R., Maskos, M., Schild, H., Stauber, R.H., 2011. Nanoparticle size is a critical physicochemical determinant of the human blood plasma corona: a comprehensive quantitative proteomic analysis. ACS nano 5, 7155-7167.

Turkevich, J., 1985. Colloidal gold. Part I. Gold Bulletin 18, 86-91.

Velasco-Aguirre, C., Morales-Zavala, F., Salas-Huenuleo, E., Gallardo-Toledo, E., Andonie, O., Munoz, L., Rojas, X., Acosta, G., Sanchez-Navarro, M., Giralt, E., Araya, E., Albericio, F., Kogan, M.J., 2017. Improving gold nanorod delivery to the central nervous system by conjugation to the shuttle Angiopep-2. Nanomedicine 12, 2503-2517.

Vera, A.M., Carcamo, J.J., Aliaga, A.E., Gomez-Jeria, J.S., Kogan, M.J., Campos-Vallette, M.M., 2015. Interaction of the CLPFFD peptide with gold nanospheres. A Raman, surface enhanced Raman scattering and theoretical study. Spectrochimica acta. Part A, Molecular and biomolecular spectroscopy 134, 251-256.

Weissleder, R., 2001. A clearer vision for in vivo imaging. Nat Biotechnol 19, 316-317.

Wu, J., Ding, T., Sun, J., 2013. Neurotoxic potential of iron oxide nanoparticles in the rat brain striatum and hippocampus. Neurotoxicology 34, 243-253.

Xue, J., Liu, T., Liu, Y., Jiang, Y., Seshadri, V.D.D., Mohan, S.K., Ling, L., 2019. Neuroprotective effect of biosynthesised gold nanoparticles synthesised from root extract of Paeonia moutan against Parkinson disease - In vitro &In vivo model. Journal of photochemistry and photobiology. B, Biology 200, 111635.

Ye, D., Zhang, X., Yue, Y., Raliya, R., Biswas, P., Taylor, S., Tai, Y.C., Rubin, J.B., Liu, Y., Chen, H., 2018. Focused ultrasound combined with microbubble-mediated intranasal delivery of gold nanoclusters to the brain. Journal of controlled release : official journal of the Controlled Release Society 286, 145-153.

Yin, N., Yao, X., Zhou, Q., Faiola, F., Jiang, G., 2015a. Vitamin E attenuates silver nanoparticle-induced effects on body weight and neurotoxicity in rats. Biochemical and biophysical research communications 458, 405-410.

Yin, N., Zhang, Y., Yun, Z., Liu, Q., Qu, G., Zhou, Q., Hu, L., Jiang, G., 2015b. Silver nanoparticle exposure induces rat motor dysfunction through decrease in expression of calcium channel protein in cerebellum. Toxicology letters 237, 112-120.

Ze, Y., Zheng, L., Zhao, X., Gui, S., Sang, X., Su, J., Guan, N., Zhu, L., Sheng, L., Hu, R., Cheng, J., Cheng, Z., Sun, Q., Wang, L., Hong, F., 2013. Molecular mechanism of titanium dioxide nanoparticles-induced oxidative injury in the brain of mice. Chemosphere 92, 1183-1189.

Zhu, G., Zhu, X., Fan, Q., Wan, X., 2011. Raman spectra of amino acids and their aqueous solutions. Spectrochimica acta. Part A, Molecular and biomolecular spectroscopy 78, 1187-1195.

Figure captions

Fig. 1. Report summary. (a) Gold nanospheres and nanoprisms functionalized both HS-PEG-COOH and D1 peptide (GNS-D1 and GNPr-D1, respectively) were physiochemically characterized. (b) Evaluation of cell proliferation in BV-2 microglial cells at different concentrations of GNS-D1 and GNPr-D1. (c) GNS-D1 and GNPr-D1 were administered by the IN route to compare the amounts of gold found in brain, olfactory bulbs, and plasma. (d) Larger amount of gold was found in brain when GNS-D1 were administered, therefore, a pharmacokinetic study was performed with this nanosystem. Results showed that the brain peak level was reached after 45min. Finally, a comparison between IN and IV administrations were carried out to determine the accumulation and distribution of gold in brain and body organs.

Fig. 2. Characterization of the GNPr functionalization steps from GNPr to GNPr-D1. (a) Normalized absorbance spectra of GNPr, GNPr-PEGx2, and GNPr-D1. (b), (c), and (d) show TEM images of GNPr after synthesis, GNPr-PEGx2, and GNPr-D1, respectively. Histograms show the size distribution and the length's mean after each step of functionalization.

Fig. 3. Summary of GNPr-PEG's enrichment process. (a) Normalized absorbance spectra for GNPr-PEG, from P1 to P6, where a displacement of the plasmon band to NIR is observed as GNPr-PEG are centrifuged and resuspended. (b) Image for GNPr-PEG P1 (left) and GNPr-PEG P6 (right). Both samples have the same absorbance for the NIR plasmon. (c) and (d) TEM images from enrichment process for P1 and P6, respectively. Each sample was analyzed, and its respective size distribution histogram and mean length was calculated.

Fig. 4. Characterization of GNS functionalization steps from GNS to GNS-D1. (a) Normalized absorbance spectra for GNS, GNS-PEG, and GNS-D1. (b), (c), and (d) show TEM images for GNS, GNS-PEG, and GNS-D1, respectively. All samples were stained with 1% phosphotungstic acid. Size distribution and mean diameter were measured taking into consideration the "halo" around the surface.

Fig. 5. Disposition of D1 peptide over the gold surface. (a) Raman spectrum of D1 peptide (i), GNS-D1 (ii) and GNPr-D1 (iii). (b) Schematic representation of the disposition of D1 over the surface of GNPr-D1 (left) and GNS-D1 (right).

Fig. 6. XTT viability assay on BV-2 cells. Results are expressed as % of cell viability (relative to medium control) after 24 h incubation with GNPr-D1 (a) or GNS-D1 (b) at various concentrations of gold

nanoparticles. Results are presented as mean ± standard deviation of 3 independent experiments (triplicate). **p < 0.05, One-way ANOVA, Kruskal-Wallis.

Fig. 7. Gold quantification at 0.5 h after IN administration of GNPr-D1 or GNS-D1. Gold was found in brain (a), olfactory bulbs (b), and plasma (c). The amount of gold found in brain after use GNPr-D1 or GNS-D1 was significantly different. * = $p < 0.05$, Student's T-test, n = 3. Results are represented as mean ± SEM.

Fig. 8. Pharmacokinetic profiles of gold after IN administration of GNS-D1. Gold levels were determined in brain (a), olfactory bulbs (b), plasma (c) and liver (d) at 0.75, 2, 4, 8, and 24 h after IN administration of GNS-D1. Results are represented as mean ± SEM.

Fig. 9. Gold quantification 0.75 h after IN or IV administration of GNS-D1. Gold accumulations were analyzed in brain (a), olfactory bulbs (b), plasma (c), liver (d), spleen (e), and lungs (f). For brain ** = $p < 0.01$, and for the rest of organs * = $p < 0.05$, Student's T-test, n = 3. Results are represented as mean ± SEM.

Fig. 10. Brain distribution of GNS-D1 0.75 h after IN or IV administrations. Brain was fixed and sectioned (coronary plane) from olfactory bulbs to cerebellum. GoldEnhance™ for light microscopy was used to determined and compared GNS-D1 localization. Representative schemes show the biodistribution of GNS-D1 in different coronary planes: (a) +9.18 mm, (b) +1.99 mm, (c) -0.2 mm, (d) -3.32 mm, (e) -6.76 mm, and (f) -10.82 mm *ant Bregma*. Red and green dots correspond to IN and IV gold clusters, respectively. Images obtained by light microscopy for IN administration are shown as example for each section analyzed.

Authors' contributions

E.G. performed most of the experiments, drafted the manuscript, and prepared figures. A.T. contributed to the synthesis, purification, and functionalization of GNPr and the discussion of the results. F.C. conducted Raman spectroscopy experiments to determine the disposition of D1 peptide over the gold surface and wrote down the corresponding section in the manuscript. T.S. carried out the cell proliferation assays in BV-2 cells. M.C. directed Raman spectroscopy analysis and facilitated the equipment. M.K. and A.S. directed the thesis research, planned the manuscript, and helped write down and edit the manuscript and figures. A.S. performed administrations for most of the *in vivo* experiments.

Declaration of interests

☒ The authors declare that they have no known competing financial interests or personal relationships that could have appeared to influence the work reported in this paper.

☐The authors declare the following financial interests/personal relationships which may be considered as potential competing interests:

Highlights

- GNS-D1 exhibit a higher uptake to the brain than GNPr-D1 after intranasal administration.
- Two phases of gold absorption to brain were observed after intranasal administration of GNS-D1.
- Intranasal administration improves the delivery of GNS-D1 to the brain and avoids systemic exposure.
- GNS-D1 distribution in the brain was similar after intranasal or after intravenous administration.